Aberration-corrected large-scale hybrid metalenses

Research Article Vol. 8, No. 11 / November 2021 / Optica 1405

Aberration-corrected large-scale hybrid metalenses

Rajath Sawant,[1] Daniel Andrén,[2] Renato Juliano Martins,[1] Samira Khadir,[1] Ruggero Verre,[2] Mikael Käll,[2] and Patrice Genevet[1,*]

[1]Université Cote d'Azur, CNRS, CRHEA, Rue Bernard Gregory, Sophia Antipolis 06560 Valbonne, France
[2]Department of Physics, Chalmers University of Technology, 412 96 Göteborg, Sweden
*Corresponding author: Patrice.Genevet@crhea.cnrs.fr

Received 22 June 2021; revised 6 September 2021; accepted 12 September 2021 (Doc. ID 434040); published 3 November 2021

Hybrid components combining the optical power of a refractive and a diffractive optical system can form compact doublet lenses that correct various aberrations. Unfortunately, the diffraction efficiency of these devices decreases as a function of the deflection angle over the element aperture. Here, we address this issue, compensating for chromatic dispersion and correcting for monochromatic aberrations with centimeter-scale hybrid-metalenses. We demonstrate a correction of at least 80% for chromatic aberration and 70% for spherical aberration. We finally present monochromatic and achromatic images that clearly show how these hybrid systems outperform standard refractive lenses. The possibilities to adjust arbitrary spatial amplitude, phase, polarization, and dispersion profiles with hybrid metasurfaces offer unprecedented optical design opportunities for compact and broadband imaging, augmented reality/virtual reality, and holographic projection.

https://doi.org/10.1364/OPTICA.434040

1. INTRODUCTION

Refractive lenses are extensively used in imaging systems such as cameras, microscopes, and telescopes. The ability of lenses to converge or diverge the optical ray trajectories is conferred to the material by its curvature and thickness. Lenses with high refractive power, defined as $P = 1/f$, where f is the focal distance of the lens, require thick high-refractive-index materials and/or large curvatures, imposing strong limitations due to costly materials and/or complex fabrication processes, involving material cutting, grinding, and polishing. Besides these technical issues, most of the refractive components suffer from optical aberrations, generally classified in two main categories, namely monochromatic and chromatic. This results in distorted images, limiting the resolution and performance of imaging systems. The conventional solution to correct for the aberrations is to cascade multiple refractive optical elements along the beam trajectory, where each optical element has a different shape and material properties to correct a given aberration. However, such schemes result in massive, bulky, and costly lens systems, of a few hundred grams and with centimeter thickness.

Ubiquitous in portable electronics and other embedded technologies, conventional lenses do not fit anymore in the compact devices. Efforts to reduce the size while keeping high performance, including the use of diffractive optical elements (DOE), has led to the realization of composite or hybrid optical devices, benefitting from the significant negative dispersion caused by the diffractive optics, to mitigate chromatic dispersion of glass lenses and holograms [1].

Hybrid diffractive-refractive achromats have been proposed. Their performances are analyzed using theoretical and numerical modeling given by the Abbe V-number relationships between the lens and diffractive optics [2,3]. Going beyond achromatic response, the spherical phase function of a diffractive element can be replaced by a complex aspherical phase distribution to treat spherical aberration as well. Further optimization of the diffractive optical structure could improve the performance of the hybrid devices, at the cost of numerical optimization. Dielectric and semiconductor metasurfaces for visible wavelengths are promising candidates to overcome the limitations of diffractive optics [4–9]. Interesting metalens designs that mitigate their inherent diffractive dispersion, also called achromatic metalenses, have been proposed [10–12]. Several different solutions have been implemented, including interleaved meta-molecules [13], dispersive antennas to address the group delay and group delay dispersion [14,15], or using multilayer metasurfaces [16]. However, all of these "dispersion phase engineering methods" have strong fundamental limitations, leading to an inevitable trade-off between the actual phase dispersion of the building blocks and the metalens performance (focusing efficiency, NA, bandwidth, and physical size of the component) [17]. To overcome these limitations, millimeter-sized large metacorrectors for lens aberration have also been demonstrated using dispersion compensated coupled dielectric nanofins [18,19]. Other approaches such as dual-layer metalenses [20,21], metasurfaces composed of nanorings for wide-angle imaging [22], multilevel diffractive lenses [23], or phase plate–metasurface hybrid components [24,25] are proposed. Nevertheless, designing large-area devices with these techniques can be computationally expensive. Also, efforts to unearth clear limitations of metalens' Fresnel number for diffraction-limited and high efficiency broadband lenses have been done [26,27].

In this paper, we propose to realize experimentally a centimeter-scale aberration-compensated optical system, more suitable for commercial applications, using a hybrid refractive-diffractive metasurface approach. A single metalens already corrects for spherical aberration [28]. Here, we show that its combination with existing refractive optics can compensate for both spherical and chromatic aberration of a refractive commercial lens system. The properties of the metasurface devices are engineered to correct the aberrations of a classical positive spherical lens, in agreement with previous calculations on hybrid diffractive-refractive achromats [3]. Two metasurfaces, correcting either for chromatic or spherical aberrations, with different properties are considered. The article is organized as follows: the first part introduces the design, fabrication, and characterization procedures of the metacorrectors, where we first derive the phase profiles needed to correct for chromatic and spherical aberrations. Then, we describe the fabrication method to realize the large-scale designed metacorrectors and present the experimental characterization results of the metacorrectors, including conversion efficiencies and phase profiles. In the second part, the hybrid diffractive-refractive device based on a combination of the metacorrector with a classical plano–convex lens is analyzed. We then present the characterization results, including point-spread function (PSF), aberration coefficients, and imaging, demonstrating up to 80% and 70% of chromatic and spherical aberration correction, respectively.

2. METALENS COMPENSATOR DESIGNS, FABRICATION, AND CHARACTERIZATION

The inherent chromatic aberration of a given plano–convex lens can be compensated by conceiving a metasurface with negative (diffractive) dispersion. Our derivation uses the generalized law of refraction [29] applied to the combination of metasurface and refractive lens [30]. As shown in Supplement 1, this calculation is adapted for both cases of achromatic and monochromatic aberrations such as spherical aberration. This work is essentially the metasurface counterpart of previous doublet and triplet optical systems traditionally used for aberration-corrected imaging systems. In our case, the metasurface (or metacorrector) is fabricated on a substrate, which is later placed on the planar surface of a plano–convex lens to compensate for the aberrations (see Fig. S1 in Supplement 1). With respect to the general calculations in [3] used to calculate the diffractive phase profile, here we consider ray optics propagation across a refractive dispersive lens approximating its material dispersion from first-order Taylor expansion around the design wavelength. Our calculations show that the metasurface phase delaying profiles should follow the expressions in Eqs. (1) and (2) (see additional information and previous works [30], in good agreement with the expression 11 in [3]):

chromatic aberration correction (CAC):

$$\varphi = -\frac{2\pi B r^2}{\lambda_0^3 R}, \tag{1}$$

spherical aberration correction:

$$\varphi = -\frac{2\pi}{\lambda_0}\left(\sqrt{f^2+r^2} + \frac{1}{R^2}\left[\left((n^2R^2-(r+k)^2)^{\frac{3}{2}} - (R^2-(r+k)^2)^{\frac{3}{2}}\right) * \frac{1}{3}\left(1 - \frac{d(n-1)}{nR} + \frac{3(r+k)^2(n-1)}{2nR^2}\right) + \frac{(n-1)}{5nR^2}\left((n^2R^2-(r+k)^2)^{\frac{5}{2}} - (R^2-(r+k)^2)^{\frac{5}{2}}\right)\right]\right), \tag{2}$$

where

$$k = \left(d - \frac{r^2}{2R}\right)(n-1)r/(nR).$$

Here B is the second Cauchy's coefficient, r is the radial coordinate of the metasurface, λ_0 is the design wavelength, and R is the radius of curvature of the plano–convex lens. f and n are the lens focal length and refractive index of the lens material at the design wavelength 650 nm, respectively, and d the central thickness of the lens.

To perform the calculations, we consider a fused silica plano–convex lens with a half-in. aperture diameter, a 50 mm focal length (for $\lambda = 600$ nm), and 23 mm radius of curvature. The metacorrectors are made of 1 cm diameter metasurfaces placed on the planar side of the refractive lens. To neglect the potential resonant phase dispersion in the building blocks, we address the overall component dispersion phase profile using Pancharatnam–Berry (PB) phase [31]. Due to the properties of PB antennas, the phase delay profiles are encoded in cross circular polarization terms by locally orienting the asymmetric metasurface building blocks at angles equal to half the local phase shift. Note that, due to the PB phase encoding technique, which utilizes only one nanostructure design, it does not introduce additional spatially varying phase dispersion. However, it adds only a constant phase dispersion for all antenna across the whole interface, as shown in Fig. SI 9 in Supplement 1. Group delay and group delay dispersion would have to be considered for other phase addressing techniques. Two metacorrectors, chromatic aberration correction metasurface (CAM) and spherical aberration correction metasurface (SAM) are fabricated encoding the phase delay profiles of Eqs. (1) and (2), respectively.

Centimeter-scale metasurfaces were realized by employing a novel nanofabrication approach described in detail in [32]. A negative electron-beam resist (ma-N 2410) is used as the sole constituent material for the metasurface, thereby removing any need for further processing in terms of material deposition or etching. The resist is simply spin-coated onto the substrate and exposed to cross-link during an electron-beam lithography step, and subsequently the metasurface is uncovered by submersion in a chemical developer. It yields high aspect ratio nanofins functioning as PB phase meta-atoms. This technique allows for relatively fast construction of large-scale metasurfaces and can produce efficient metasurfaces in the visible wavelength regime [32]. A square unit cell with the side length of 440 nm is chosen so as to suppress all the diffraction orders between two adjacent pillars (both transmissive and reflective) at the design wavelength. In each unit cell, a nanofin with dimensions of $350 \times 100 \times 1700$ nm^3 is placed, and the entire metacorrector is subsequently composed of nanofins whose orientation angles are chosen to impart the desired phase profile.

The fabricated metacorrectors are experimentally characterized to validate the theoretical design as illustrated in Figs. 1(a) and 1(b). We show in Fig. 1(c) the comparison between simulated (Lumerical FDTD method) and measured polarization conversion efficiency spectra for the metacorrector building blocks, demonstrating a good agreement. We note that the overall device

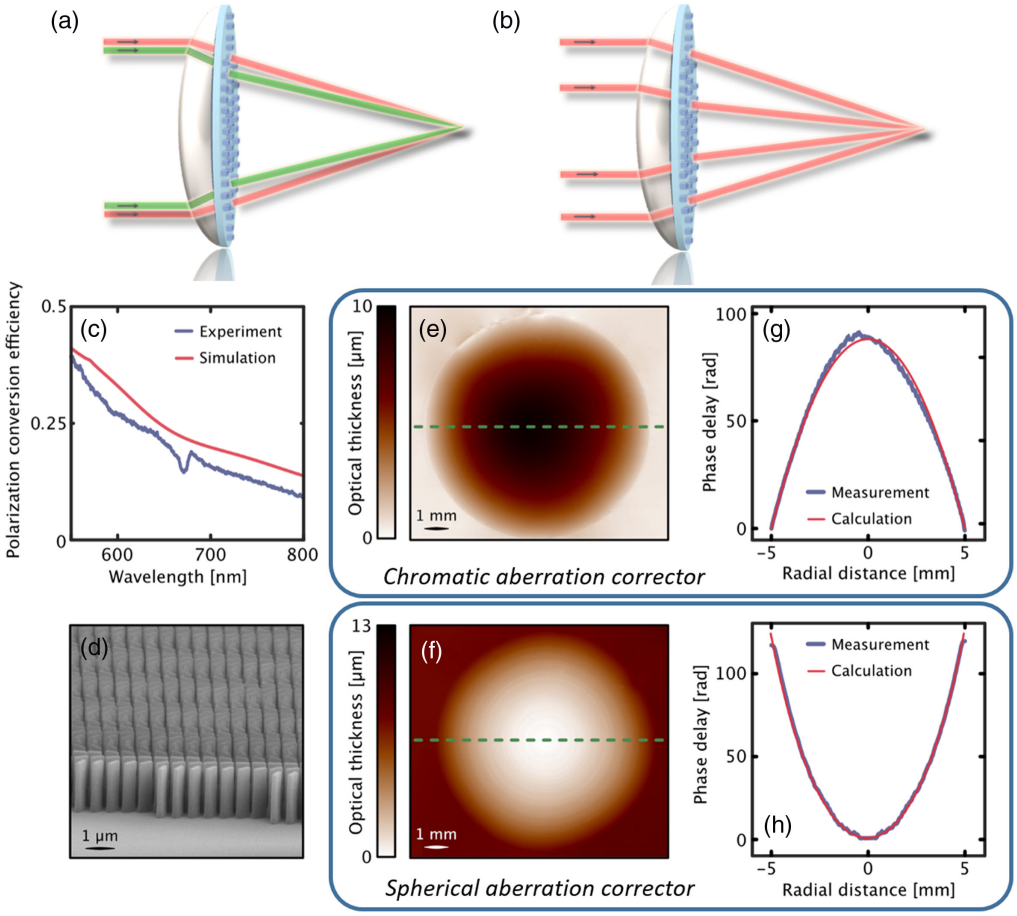

Fig. 1. Schematic of hybrid lens-metacorrector for (a) chromatic aberration correction and (b) spherical aberration correction. (c) Comparison between calculation and experimentally measured polarization conversion efficiencies as a function of incident wavelength for Pancharatnam–Berry phase nanopillars. Numerical calculations are performed using one unit cell with periodic boundary conditions and experimental measurements have been performed on a metasurface composed of sea of identical meta-atoms oriented at 45° and placed in between two crossed polarizers. (d) Scanning electron microscopy (SEM) images of large-area metasurfaces. Phase measurement results of (e) chromatic aberration correction metasurface (CAM) and (f) spherical aberration correction metasurface (SAM); (g) and (h) radially averaged phase profile [shown as green dashed lines in (e), (f)] of CAM and SAM, respectively, both measured and calculated.

efficiency of the fabricated metasurface is around 10–25% in the wavelength range of 600 to 800 nm. Figure 1(d) shows an SEM image of a segment of the fabricated metacorrector, consisting of high quality and high aspect ratio nanofins with minimum tapering. Moreover, we also performed direct phase measurements to capture the experimental phase (φ) maps, or equivalently optical path difference (OPD, where $\mathrm{OPD} = \lambda\varphi/2\pi$), at the plane of the metacorrectors using the quadriwave lateral interferometry technique (QLSI) (see Supplement 1 for more details) [33]. Figures 1(e) and 1(f) show the OPD maps of CAM and SAM, respectively. Radially averaged phase profiles are shown in Figs. 1(g) and 1(h) (blue curves), which agree with the calculated profiles by Eqs. (1) and (2) (red curves) for both cases. According to Eqs. (1) and (2), it is noticeable that CAM and SAM act differently; the former acts as a converging lens, and the latter acts as a diverging lens. This can also be inferred from their opposite sense of curvature for their phase profile as shown in Figs. 1(g) and 1(h), resulting in different focal lengths of the hybrid system with respect to the bare lens as discussed in ray tracing analysis in Fig. S3 in Supplement 1.

In addition to phase maps, QLSI captures simultaneously the intensity maps of the metacorrectors as shown in Figs. S4B and S4C in Supplement 1. Modulation in the intensity/polarization conversion is observed owing to the coupling effects between the pillars. However, it does not affect the compensation functionalities of the metasurfaces.

3. EXPERIMENTAL RESULTS OF THE HYBRID DEVICE

For qualitative and quantitative aberration measurements of lens-metasurface combination, a standard PSF measurement setup was utilized as shown in Fig. 2(a). A tunable supercontinuum laser (SCL) was used as a source, a pinhole of diameter 5 μm as a point source, a focusing lens of focal length 30 cm for collimation, and a 40×, 0.75 NA objective lens for imaging. In order to choose the diameter d of the pinhole to mimic a point source, one needs to satisfy the following condition: $d \ll \gamma\phi_{\mathrm{airy}}$ [34], with $\gamma = f_{\mathrm{FL}}/f_{\mathrm{test}}$, where $f_{\mathrm{FL}} = 200$ mm and $f_{\mathrm{test}} = 50$ mm are the focal lengths of the focusing/collimating convex lens and the test lens (CAM, SAM, or bare lens), respectively. $\phi_{\mathrm{airy}} = 2{,}44\,\lambda\,N\#$, where $\lambda = 650$ nm is the central wavelength of broadband light and $N\#$ is the f-number of the test lens. Based on these parameters, the condition on the pinhole diameter is given by $d \ll 32$ μm.

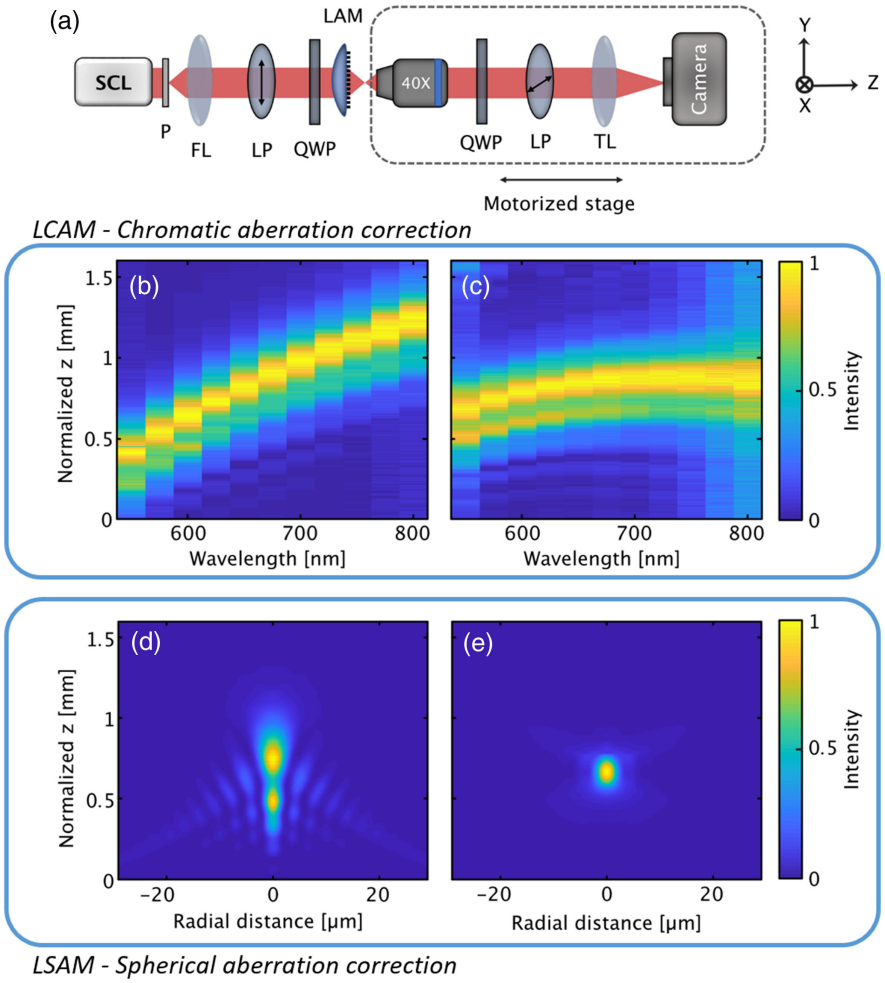

Fig. 2. (a) PSF and z-scan measurement setup: SCL, super continuum laser; P, pinhole; FL, focusing convex lens; TL, tube lens; LP, linear polarizer; QWP, quarter-wave plate; LAM, large-area metasurface (placed on the plano–convex lens). (b) Chromatic aberration characterization of the plano–convex lens by stacking z-scans for different wavelengths ranging from 550 to 800 nm with intervals of 25 nm. Intensity is normalized for each wavelength. (c) The same study for the lens-metasurface combination (LCAM). Z-scan at 650 nm wavelength for (d) plano–convex lens and (e) LSAM.

Thus, we selected a pinhole with a diameter of 5 μm for the PSF measurements.

Linear and quarter-wave plates were used to obtain left circular polarization (LCP) in the incidence and to collect only the cross-polarized right circular polarization (RCP) term. The imaging parts of the setup including objective lens, tube lens, and CMOS camera (Thorlabs) were placed on a motorized stage for scanning along the optical axis (Oz) around the focal plane of the test lens. To analyze the chromatic aberration effect of the Lens-CAM (LCAM) combination, a z-scan is performed for different incident wavelengths ranging from 550 nm to 800 nm with an interval of 25 nm. Figures 2(b) and 2(c) show a normalized intensity map as a function of the position z and the wavelength, and the z value with the highest intensity is considered as the focal plane. In the wavelength range of 600 to 800 nm, the LCAM case presents a small overall focus variation [Fig. 2(c)] as compared to that of the bare lens [Fig. 2(b)], amounting to at least 80% mitigation of chromatic aberration. Here, the CAC is calculated using the expression $\mathrm{CAC} = 1 - \frac{\Delta f_{\mathrm{hybrid}}}{\Delta f_{\mathrm{lens}}}$, where $\Delta f_{\mathrm{hybrid}}$, Δf_{lens} corresponds to difference of focal length at 600 nm and 800 nm of LCAM and lens, respectively. It can be noticed that the area around the focal plane for LCAM is broadened compared to that of the lens. This is attributed to the undesirable spherical aberration imparted by the metasurface to the system, which is discussed in the Zernike analysis section below. Similarly, a z-scan is performed with both the Lens-SAM (LSAM) and bare lens with an incident wavelength of 650 nm (design wavelength). In the case of an uncorrected lens [Fig. 2(d)], significant positive spherical aberration can be seen, whereas with LSAM [Fig. 2(e)], a much sharper, well-confined, and symmetric profile is obtained. It must be noted that the z-scan shown for LCAM and LSAM correspond to the focus from the crossed-circularly polarized first-order diffraction of the metasurface. The focus from zero-order diffraction corresponds to the light unaffected by the metasurface, which focuses similarly as the bare lens. Because of sufficient spatial separation between the 2 orders, their behavior along the optical axis can be independently measured.

To carry out the above measurements, an important condition must be verified to ensure that the PSF is sufficiently resolved in the camera. The spatial frequency that can be captured with the camera must be greater than the cutoff frequency "fc" of the diffraction-limited imaging system. We verified that the conditions are satisfied for both LCAM and LSAM, considering the modified focal length (see Supplement 1). As a quantitative

study of spherical aberration correction, the modulation transfer function of the LSAM and uncorrected lens are calculated by Fourier-transforming the PSFs [34] as compared in Fig. S5 in Supplement 1. At all spatial frequencies (lower than the cutoff frequency), LSAM showed better resolution due to mitigation of spherical aberrations. Along with it, focusing efficiencies of the hybrid components were also experimentally measured. It was found to be around 8.5% for LCAM in the wavelength range of 550 to 800 nm and around 20% for LSAM at 650 nm wavelength.

The Zernike polynomial analysis technique was employed to study geometrical aberrations (spherical aberration in our case) of an imaging system in a quantitative and comprehensive manner. This technique is based on decomposing the wavefront (i.e., deviation from the ideal case) in an orthogonal basis in such a way that the coefficients represent directly each of the lens aberrations [33,35]. To acquire the wavefront profile from the bare lens and LSAM, phase measurements based on the QLSI technique were performed, as previously described. With 617 nm LED excitation with LCP, the outgoing wavefront was captured in co-polarization configuration for the bare lens and cross-polarization configuration for the hybrid system. A circular mask or pupil size of approximately 7.5 mm in diameter was set. It is crucial to maintain the same mask size for both the bare lens and LSAM as the Zernike coefficients are quite sensitive to it. Figure 3 compares the Zernike analysis results of the lens and LSAM. Figures 3(a) and 3(b) show the OPD profiles of the bare lens and LSAM, respectively, from which the OPD profile of a perfect lens was subtracted. One can notice a considerable change in the wavefront thanks to the metasurface. From the Zernike coefficients decomposition, a drastic reduction of spherical aberration by around 70% can be seen in the case of LSAM compared to that of the bare lens. Here, the "Defocus" is set to zero as it comes from the phase profile of an ideal lens, and piston aberration is not shown as it is a constant added to the phase profile and does not affect the focus. It has to be noted that in the case of LSAM, along with spherical aberration, astigmatism and coma aberrations are also slightly reduced. Increase in the higher-order Tetrafoil aberrations can also be seen after the introduction of the metasurface. However, since they are higher-order aberrations, it does not affect the overall image quality, which can be inferred from the imaging results. The same study was carried out for LSAM when the OPD is captured with co-polarized light (LCP in both input and output). In this case, the measured wavefront corresponds to the zero-order diffraction unaffected by the metasurface in the output. The results are shown in Fig. S6 in Supplement 1. Its similarity with Zernike coefficients of the bare lens is expected, and it also verifies that the same alignment was maintained in the setup before and after the introduction of the metasurface on the lens. To quantify geometrical aberrations (apart from chromatic aberrations) of LCAM, Zernike analysis was carried out for LCAM and compared to the bare lens. An increase of around 20% in the lens' spherical aberration was found, according to Fig. S7 in Supplement 1, which explains the broadening of the focal region in Fig. 2(c). The increase of spherical aberrations is expected since the curvatures of phase profiles needed to correct for spherical and chromatic aberration are inverted (see Fig. 1).

For the overall assessment of the aberration correction from the metasurface, imaging with the LCAM and LSAM was carried out with the standard 1951 US AirForce (USAF) resolution target. To verify CAC, a SCL was used to generate a broadband light (wavelength range set to 550–800 nm) as shown in Fig. 4(a). For imaging, the Thorlabs Zelux CMOS color camera (1.6 MP) was employed, color coding in magenta all wavelengths in the infrared region of the spectrum above 750 nm. By comparing Figs. 4(b) and 4(c) showing group 3 of the target, one can notice sharper images

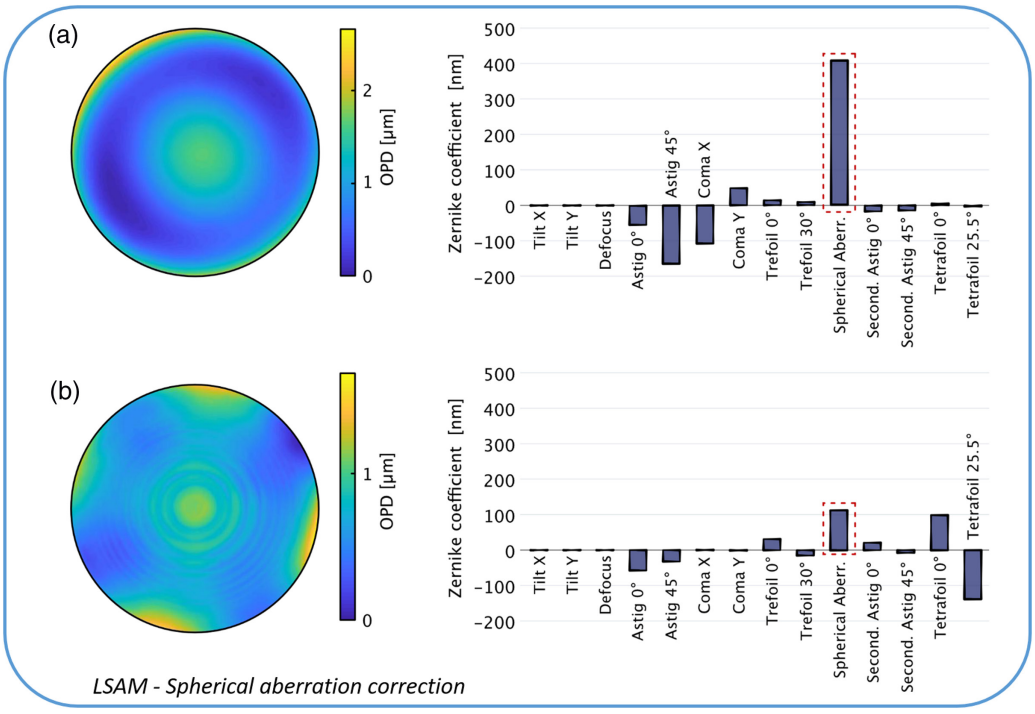

Fig. 3. (a) Optical thickness and Zernike coefficients measured on phase measurement setup for the plano–convex lens. (b) The same measurements for the LSAM combination for the cross-polarization component. Defocus is subtracted in both cases. Aberration name in the same order as in the figures: Tilt X, Tilt Y, Defocus (= 0), Astigmatism 0°, Astigmatism 45°, Coma X, Coma Y, Trefoil 0°, Trefoil 30°, spherical aberration, secondary astigmatism 0°, secondary astigmatism 45°, Tetrafoil 0°, Tetrafoil 25.5°.

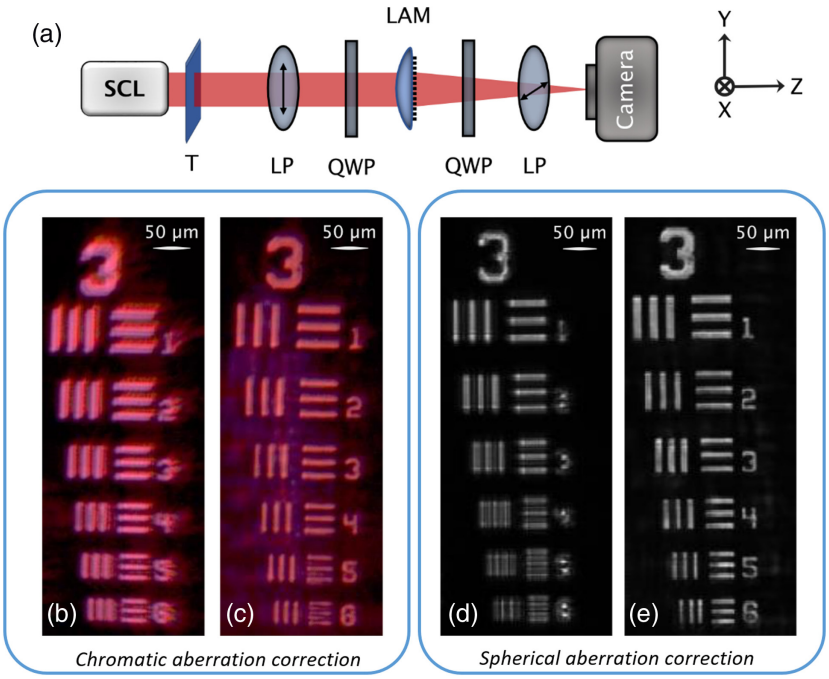

Fig. 4. (a) Single lens imaging setup: SCL, super continuum laser; T, target; LP, linear polarizer; QWP, quarter-wave plate; LAM, large-area metasurface (placed on the plano–convex lens). Imaging results with USAF target for chromatic aberration (wavelength range 550 to 800 nm) with (b) plano–convex lens and (c) LCAM combination. The same for spherical aberration (incident wavelength 650 nm) with (d) plano–convex lens and (e) LCAM combination. High resolution infinite-conjugate imaging was also performed to highlight the device imaging performance up to group 6 (see Supplement 1, Fig. S8).

because of chromatic aberration mitigation with the LCAM. However, the background light can be seen in Fig. 4(c), which is a result of incomplete filtering out of the co-polarized component of broadband light. Also, it has to be noted that spherical aberration is still present in the LCAM system. Similarly, to test the imaging capabilities of the LSAM, the wavelength of the source is set to be quasi-monochromatic at 650 nm (design wavelength) with a bandwidth of 10 nm. Here, instead, a Thorlabs CMOS camera, DCC1545M monochrome, is used as a detector. Images with higher resolution are obtained with the LSAM [Fig. 4(e)] in comparison to the bare lens [Fig. 4(d)], indicating that spherical aberration is mitigated with the metasurface. High resolution infinite-conjugate imaging results of group 6 and 7 elements are shown in Fig. S8 in Supplement 1.

4. CONCLUSION

In conclusion, we have demonstrated a hybrid lens-metasurface component for aberration correction using an approach advantageous for the design of large-area metasurfaces. In these hybrid devices, the advantages of high transmission efficiency of refractive components is combined with the compactness of diffractive components. We designed two types of metacorrectors, and we demonstrated 80% and 70% reduction of chromatic and spherical aberrations, respectively, of a conventional refractive lens. In an objective lens, series of lenses with different materials and curvatures are employed to realize aberration-free imaging. By replacing the cascading lenses with flat and large-area metasurfaces, an order of magnitude miniaturization and weight reduction can be achieved, which makes these devices attractive for practical applications in particular for portable electronics. For example, they are of high interest for cell phone imaging where the thickness is continuously decreasing, as well as for augmented and virtual reality technologies requiring compact optical systems that can be implemented on conventional glasses.

It is worth noting that the polarization conversion efficiency of our PB metasurface is not very high (around 10–25%) in the wavelength range of our operation, leading to overall focusing efficiency of about 8.5%, but either the design can be optimized to reach significantly higher efficiencies [36] or an alternative fabrication platform can be used [9,37]. To position our work with the recent results published in the literature related to achromatic metalenses and metacorrectors, we have provided a comparison table in Supplement 1. It can be inferred that, in this work, a relatively large size of 1 cm diameter metacorrector is achieved with around 0.1 numerical aperture in the wavelength range of 600 to 800 nm. Such large-area devices can be fabricated in mass production lines with low cost using emerging fabrication techniques such as nanoimprint or deep UV lithography.

Funding. Knut och Alice Wallenbergs Stiftelse; European Research Council (639109).

Acknowledgment. This work was also supported by the Knut and Alice Wallenberg Foundation and the Excellence Initiative Nano at Chalmers University of Technology. The nanofabrication was performed at Myfab Chalmers. Correspondence and requests for materials should be addressed to P. G.

Disclosures. The authors declare no competing financial interests.

Data Availability. Data underlying the results presented in this paper are not publicly available at this time but may be obtained from the authors upon reasonable request.

Supplemental document. See Supplement 1 for supporting content.

REFERENCES

1. R. H. Katyl, "Compensating optical systems. Part 1: broadband holographic reconstruction," Appl. Opt. **11**, 1241–1247 (1972).

2. T. Stone and N. George, "Hybrid diffractive-refractive lenses and achromats," Appl. Opt. **27**, 2960–2971 (1988).
3. N. Davidson, A. A. Friesem, and E. Hasman, "Analytic design of hybrid diffractive-refractive achromats," Appl. Opt. **32**, 4770–4774 (1993).
4. M. Khorasaninejad, A. Y. Zhu, C. Roques-Carmes, W. T. Chen, J. Oh, I. Mishra, R. C. Devlin, and F. Capasso, "Polarization-insensitive metalenses at visible wavelengths," Nano Lett. **16**, 7229–7234 (2016).
5. P. Genevet, F. Capasso, F. Aieta, M. Khorasaninejad, and R. Devlin, "Recent advances in planar optics: from plasmonic to dielectric metasurfaces," Optica **4**, 139–152 (2017).
6. A. Arbabi, Y. Horie, M. Bagheri, and A. Faraon, "Dielectric metasurfaces for complete control of phase and polarization with subwavelength spatial resolution and high transmission," Nat. Nanotechnol. **10**, 937–943 (2015).
7. P. Lalanne, S. Astilean, P. Chavel, E. Cambril, and H. Launois, "Blazed binary subwavelength gratings with efficiencies larger than those of conventional échelette gratings," Opt. Lett. **23**, 1081–1083 (1998).
8. M. Khorasaninejad, W. T. Chen, R. C. Devlin, J. Oh, A. Y. Zhu, and F. Capasso, "Metalenses at visible wavelengths: diffraction-limited focusing and subwavelength resolution imaging," Science **352**, 1190–1194 (2016).
9. G. Brière, P. Ni, S. Héron, S. Chenot, S. Vézian, V. Brändli, B. Damilano, J.-Y. Duboz, M. Iwanaga, and P. Genevet, "An etching-free approach toward large-scale light-emitting metasurfaces," Adv. Opt. Mater. **7**, 1801271 (2019).
10. S. Wang, P. C. Wu, V. C. Su, Y. C. Lai, C. H. Chu, J. W. Chen, S. H. Lu, J. Chen, B. Xu, C. H. Kuan, T. Li, S. Zhu, and D. P. Tsai, "Broadband achromatic optical metasurface devices," Nat. Commun. **8**, 187 (2017).
11. A. Ndao, L. Hsu, J. Ha, J. H. Park, C. Chang-Hasnain, and B. Kanté, Octave bandwidth photonic fishnet-achromatic-metalens, Nat. Commun. **11**, 3205 (2020).
12. S. Wang, P. C. Wu, V. C. Su, Y. C. Lai, M. K. Chen, H. Y. Kuo, B. H. Chen, Y. H. Chen, T. T. Huang, J. H. Wang, R. M. Lin, C. H. Kuan, T. Li, Z. Wang, S. Zhu, and D. P. Tsai, "A broadband achromatic metalens in the visible," Nat. Nanotechnol. **13**, 227–232 (2018).
13. E. Arbabi, A. Arbabi, S. M. Kamali, Y. Horie, and A. Faraon, "Multiwavelength polarization-insensitive lenses based on dielectric metasurfaces with meta-molecules," Optica **3**, 628–633 (2016).
14. S. Shrestha, A. C. Overvig, M. Lu, A. Stein, and N. Yu, "Broadband achromatic dielectric metalenses," Light Sci. Appl. **7**, 85 (2018).
15. W. T. Chen, A. Y. Zhu, V. Sanjeev, M. Khorasaninejad, Z. Shi, E. Lee, and F. Capasso, "A broadband achromatic metalens for focusing and imaging in the visible," Nat. Nanotechnol. **13**, 220–226 (2018).
16. Y. Zhou, I. I. Kravchenko, H. Wang, J. R. Nolen, G. Gu, and J. Valentine, "Multilayer noninteracting dielectric metasurfaces for multiwavelength metaoptics," Nano Lett. **18**, 7529–7537 (2018).
17. A. C. Overvig, S. Shrestha, S. C. Malek, M. Lu, A. Stein, C. Zheng, and N. Yu, "Dielectric metasurfaces for complete and independent control of the optical amplitude and phase," Light Sci. Appl. **8**, 92 (2019).
18. W. T. Chen, A. Y. Zhu, and F. Capasso, "Flat optics with dispersion-engineered metasurfaces," Nat. Rev. Mater. **5**, 604–620 (2020).
19. W. T. Chen, A. Y. Zhu, J. Sisler, Y. W. Huang, K. M. A. Yousef, E. Lee, C. W. Qiu, and F. Capasso, "Broadband achromatic metasurface-refractive optics," Nano Lett. **18**, 7801–7808 (2018).
20. M. Li, S. Li, L. K. Chin, Y. Yu, D. P. Tsai, and R. Chen, "Dual-layer achromatic metalens design with an effective Abbe number," Opt. Express **28**, 26041–26055 (2020).
21. A. Arbabi, E. Arbabi, S. M. Kamali, Y. Horie, S. Han, and A. Faraon, "Miniature optical planar camera based on a wide-angle metasurface doublet corrected for monochromatic aberrations," Nat. Commun. **7**, 13682 (2016).
22. C. Hao, S. Gao, Q. Ruan, Y. Feng, Y. Li, J. K. W. Yang, Z. Li, and C. W. Qiu, "Single-layer aberration-compensated flat lens for robust wide-angle imaging," Laser Photon. Rev. **14**, 2000017 (2020).
23. S. Banerji, M. Meem, A. Majumder, F. G. Vasquez, B. Sensale-Rodriguez, and R. Menon, "Imaging with flat optics: metalenses or diffractive lenses?" Optica **6**, 805–810 (2019).
24. F. Balli, M. Sultan, S. K. Lami, and J. T. Hastings, "A hybrid achromatic metalens," Nat. Commun. **11**, 3892 (2020).
25. F. Balli, M. A. Sultan, A. Ozdemir, and J. T. Hastings, "An ultrabroadband 3D achromatic metalens," Nanophotonics **10**, 1259–1264 (2021).
26. J. Engelberg and U. Levy, "Achromatic flat lens performance limits," Optica **8**, 834–845 (2021).
27. F. Presutti and F. Monticone, "Focusing on bandwidth: achromatic metalens limits," Optica **7**, 624–631 (2020).
28. F. Aieta, P. Genevet, M. A. Kats, N. Yu, R. Blanchard, Z. Gaburro, and F. Capasso, "Aberration-free ultrathin flat lenses and axicons at telecom wavelengths based on plasmonic metasurfaces," Nano Lett. **12**, 4932–4936 (2012).
29. N. Yu, P. Genevet, M. A. Kats, F. Aieta, J.-P. Tetienne, F. Capasso, and Z. Gaburro, "Light propagation with phase discontinuities: generalized laws of reflection and refraction," Science **334**, 333–337 (2011).
30. R. Sawant, P. Bhumkar, A. Y. Zhu, P. Ni, F. Capasso, and P. Genevet, "Mitigating chromatic dispersion with hybrid optical metasurfaces," Adv. Mater. **31**, 1805555 (2019).
31. Z. Bomzon, G. Biener, V. Kleiner, and E. Hasman, "Space-variant Pancharatnam–Berry phase optical elements with computer-generated subwavelength gratings," Opt. Lett. **27**, 1141–1143 (2002).
32. D. Andrén, J. Martínez-Llinàs, P. Tassin, M. Käll, and R. Verre, "Large-scale metasurfaces made by an exposed resist," ACS Photon. **7**, 885–892 (2020).
33. S. Khadir, D. Andrén, R. Verre, Q. Song, S. Monneret, P. Genevet, M. Käll, and G. Baffou, "Metasurface optical characterization using quadriwave lateral shearing interferometry," ACS Photon. **8**, 603–613 (2021).
34. A. Vernier, B. Perrin, T. Avignon, J. Augereau, and L. Jacubowiez, "Measurement of the modulation transfer function (MTF) of a camera lens," in *Edu. Train. Opt. Photonics* (2015), paper TPE28.
35. V. Lakshminarayanan and A. Fleck, "Zernike polynomials: a guide," J. Mod. Opt. **58**, 545–561 (2011).
36. G. Zheng, H. Mühlenbernd, M. Kenney, G. Li, T. Zentgraf, and S. Zhang, "Metasurface holograms reaching 80% efficiency," Nat. Nanotechnol. **10**, 308–312 (2015).
37. R. C. Devlin, M. Khorasaninejad, W. T. Chen, J. Oh, and F. Capasso, "Broadband high-efficiency dielectric metasurfaces for the visible spectrum," Proc. Natl. Acad. Sci. USA **113**, 10473–10478 (2016).